



Observation and Modeling of Chromospheric Evaporation in a Coronal Loop Related to Active Region Transient Brightening

G. R. Gupta^{1,3} , Aavek Sarkar² , and Durgesh Tripathi¹

¹ Inter-University Centre for Astronomy and Astrophysics, Post Bag-4, Ganeshkhind, Pune 411007, India; girjesh@iucaa.in

² Physical Research Laboratory, Navrangpura, Ahmedabad 380009, India

Received 2017 October 16; revised 2018 March 19; accepted 2018 March 21; published 2018 April 25

Abstract

Using the observations recorded by the Atmospheric Imaging Assembly (AIA) on board the *Solar Dynamics Observatory* and the *Interface Region Imaging Spectrograph* (IRIS) and the Extreme-ultraviolet Imaging Spectrometer and X-Ray Telescope both on board *Hinode*, we present evidence of chromospheric evaporation in a coronal loop after the occurrence of two active region transient brightenings (ARTBs) at the two footpoints. The chromospheric evaporation started nearly simultaneously in all of the three hot channels of AIA 131, 94, and 335 Å and was observed to be temperature dependent, being fastest in the highest temperature channel. The whole loop became fully brightened following the ARTBs after ≈ 25 s in 131 Å, ≈ 40 s in 94 Å, and ≈ 6.5 minutes in 335 Å. The differential emission measurements at the two footpoints (i.e., of two ARTBs) and at the loop top suggest that the plasma attained a maximum temperature of ~ 10 MK at all these locations. The spectroscopic observations from IRIS revealed the presence of redshifted emission of ~ 20 km s⁻¹ in cooler lines like C II and Si IV during the ARTBs that was cotemporal with the evaporation flow at the footpoint of the loop. During the ARTBs, the line width of C II and Si IV increased nearly by a factor of two during the peak emission. Moreover, enhancement in the line width preceded that in the Doppler shift, which again preceded enhancement in the intensity. The observed results were qualitatively reproduced by 1D hydrodynamic simulations, where energy was deposited at both of the footpoints of a monolithic coronal loop that mimicked the ARTBs identified in the observations.

Key words: hydrodynamics – Sun: corona – Sun: flares – Sun: transition region – Sun: UV radiation

1. Introduction

Active region transient brightenings (ARTBs; Shimizu et al. 1992) are small, intense events occurring in or near the active regions and were first studied using a sequence of images recorded by the Soft X-ray Telescope (SXT; Tsuneta et al. 1991) on board *Yohkoh*. These events are mainly found in active regions, on average, every 3 minutes and have various morphologies like single-point or multiple-point brightening. ARTBs have also been observed with simultaneous multiloop brightenings or even jets (Shimizu et al. 1994; Chandrashekar et al. 2014; Mulay et al. 2016). Moreover, they have been observed as precursors to prominence eruptions (e.g., Chifor et al. 2006, 2007; Tripathi et al. 2006), prominence oscillations (e.g., Isobe & Tripathi 2006; Tripathi et al. 2009a), and so on. They may play an important role in the heating of solar corona (Yokoyama & Shibata 1995). Therefore, it is imperative to fully comprehend the thermodynamics involved in such events with the aid of modern high-resolution imaging and spectroscopic observations and modeling.

Berghmans et al. (2001) investigated the correspondence between X-ray observations of ARTBs with extreme ultraviolet (EUV) brightening. They found that the strongest ARTBs observed in the EUV had a counterpart in X-rays, whereas weaker EUV ARTBs did not show any X-ray emission. This was attributed to the fact that no plasma is heated beyond 2 MK. Since the energy values of ARTBs were similar to that of microflares, which are six orders of magnitude lower than a flare, ARTBs are also referred to as microflares (see, Hudson et al.

2004). Hereafter, we shall be using the microflare and ARTB terms interchangeably.

Using the hard X-ray observations recorded by the *Reuven Ramaty High Energy Solar Spectroscopic Imager* (RHESSI; Lin et al. 2002), Christe et al. (2008) performed a detailed statistical study of microflares and obtained frequency distributions of the peak energy (see also Régnier et al. 2014; Subramanian et al. 2018, using Hi-C and Atmospheric Imaging Assembly (AIA) observations). These distributions can be represented by power-law distributions with a negative power-law index between 1.5 and 1.6. Such distributions suggest that the process of energy release in microflares is similar to those in large flares, though the energy involved is about six orders of magnitude less. The process of the energy release in such microflaring events or flaring events can be summarized as follows.

At the time of impulsive energy release in (micro)flares, local chromospheric material gets heated up to very high temperatures of ≈ 10 MK. This leads to an increase in local pressure that drives the local chromospheric material upward into the corona along the (micro)flare loops. This process of filling of the loop with hot plasma is called “chromospheric evaporation” (Milligan & Dennis 2009; Li et al. 2017, and references therein). The concept of chromospheric evaporation has been successfully used to explain the loop-top brightening in postflare loops (see, e.g., Sharma et al. 2016) as well as coronal loops in general (Klimchuk 2006). Along with this, high pressure also pushes denser plasma downward into the lower chromosphere, which is referred to as “chromospheric condensation” (Milligan et al. 2006 and references therein). In such models, emissions from hot materials from the corona are expected to show blueshift (upflow), and those from cool

³ Current address: DAMTP, CMS, University of Cambridge, Wilberforce Road, Cambridge CB3 0WA, UK; gg454@cam.ac.uk

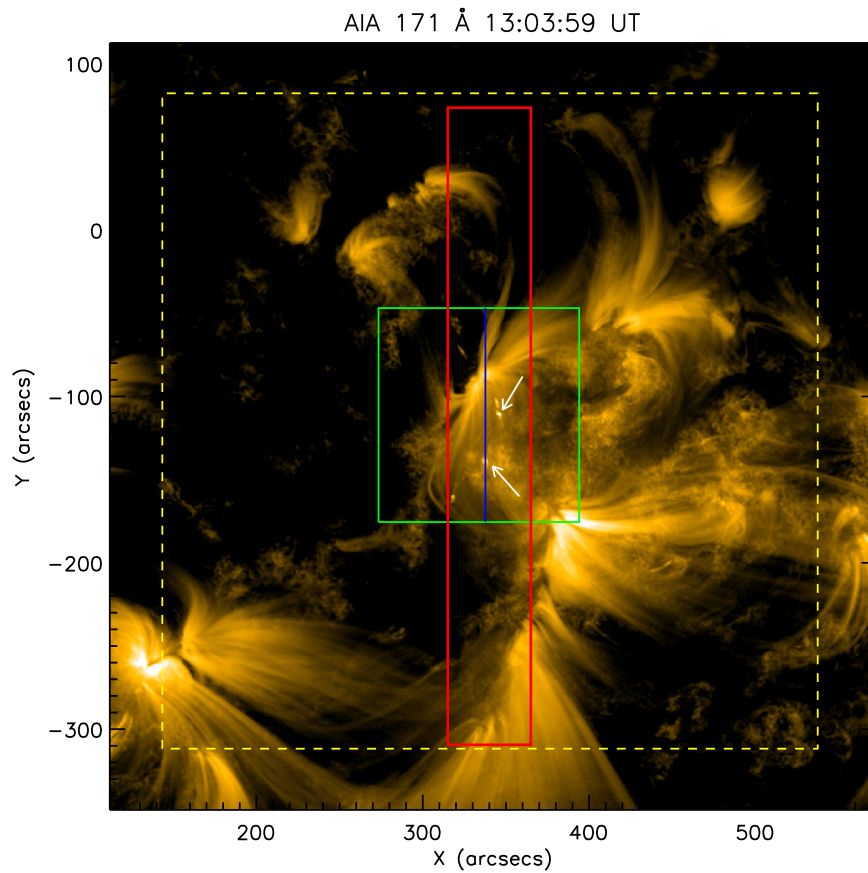


Figure 1. AIA 171 Å image recorded on 2014 March 4 shows the ARTBs marked with arrows. The overplotted red and green boxes show the EIS and *IRIS*-SJI fields of view, respectively. The yellow box shows the XRT FOV. The *IRIS* slit position is shown with the vertical blue line.

material from the upper chromosphere and transition region are expected to show redshift (downflow), as reported recently in a single observation by Li et al. (2017). As the underlying chromosphere is denser than the overlying corona, the expected speed of blueshift (upflow) should be much larger (approximately an order of magnitude) than that of redshift (downflow; e.g., Fisher et al. 1985; Milligan & Dennis 2009). The spectroscopic observations do show larger blueshifts for the spectral lines formed at higher temperatures (Del Zanna et al. 2006a). Such effects have also been seen at the footpoints of loops in quiescent active regions and are interpreted as evidence of nanoflares occurring in the corona (see, e.g., Tripathi et al. 2009b; Ghosh et al. 2017, and references therein).

As the solar corona has high thermal conductivity and low plasma β , the plasma is confined within the magnetic field lines. Thus, the evolution of plasma can be well demonstrated with a 1D hydrodynamic model (see, e.g., Mariska 1987; Peres 2000; Sarkar & Walsh 2008). In the current study, we present observations of two ARTBs and associated loop brightening by AIA (Lemen et al. 2012), the *Interface Region Imaging Spectrograph* (*IRIS*; De Pontieu et al. 2014), and the Extreme-ultraviolet Imaging Spectrometer (EIS; Culhane et al. 2007) and X-Ray Telescope (XRT; Golub et al. 2007), both on board *Hinode*. Based on this observation, we set up a 1D hydrodynamic simulation to study the dynamic evolution of the coronal loop using the procedure described by Sarkar & Walsh (2008).

The rest of the paper is organized as follows. In Section 2, we present the observations of ARTBs and the associated loop. Physical properties of the event are described in Section 3. The hydrodynamic simulation of a loop and its comparison with observational results are described in Section 4. Finally, we summarize and discuss our results in Section 5.

2. Observations

The ARTB event under study occurred on 2014 March 4 at around 13:03 UT. The event was simultaneously recorded using multiple instruments, such as the AIA and the Helioseismic and Magnetic Imager (HMI; Scherrer et al. 2012; Schou et al. 2012), both on board the *Solar Dynamics Observatory* (*SDO*), EIS and XRT on board *Hinode*, and *IRIS*. *IRIS* was operating in sit-and-stare mode, while EIS was rastering the region of interest. Figure 1 displays the AIA image taken in 171 Å. Overplotted green and red boxes highlight the EIS raster and *IRIS*/SJI field of view (FOV), respectively. The XRT field of view is indicated by an overplotted dashed yellow box. The blue vertical line represents the *IRIS* slit position. The arrows mark the ARTBs, which are the subjects of this work.

In the current study, *IRIS* observations were carried out from 12:39:30 UT to 14:37:54 UT and covered a field of view of $119'' \times 119''$. The EIS raster was obtained between 13:02:20 UT and 13:20:23 UT and covered a field of view of $51'' \times 384''$ using the $1''$ slit. *IRIS* obtained spectra in the

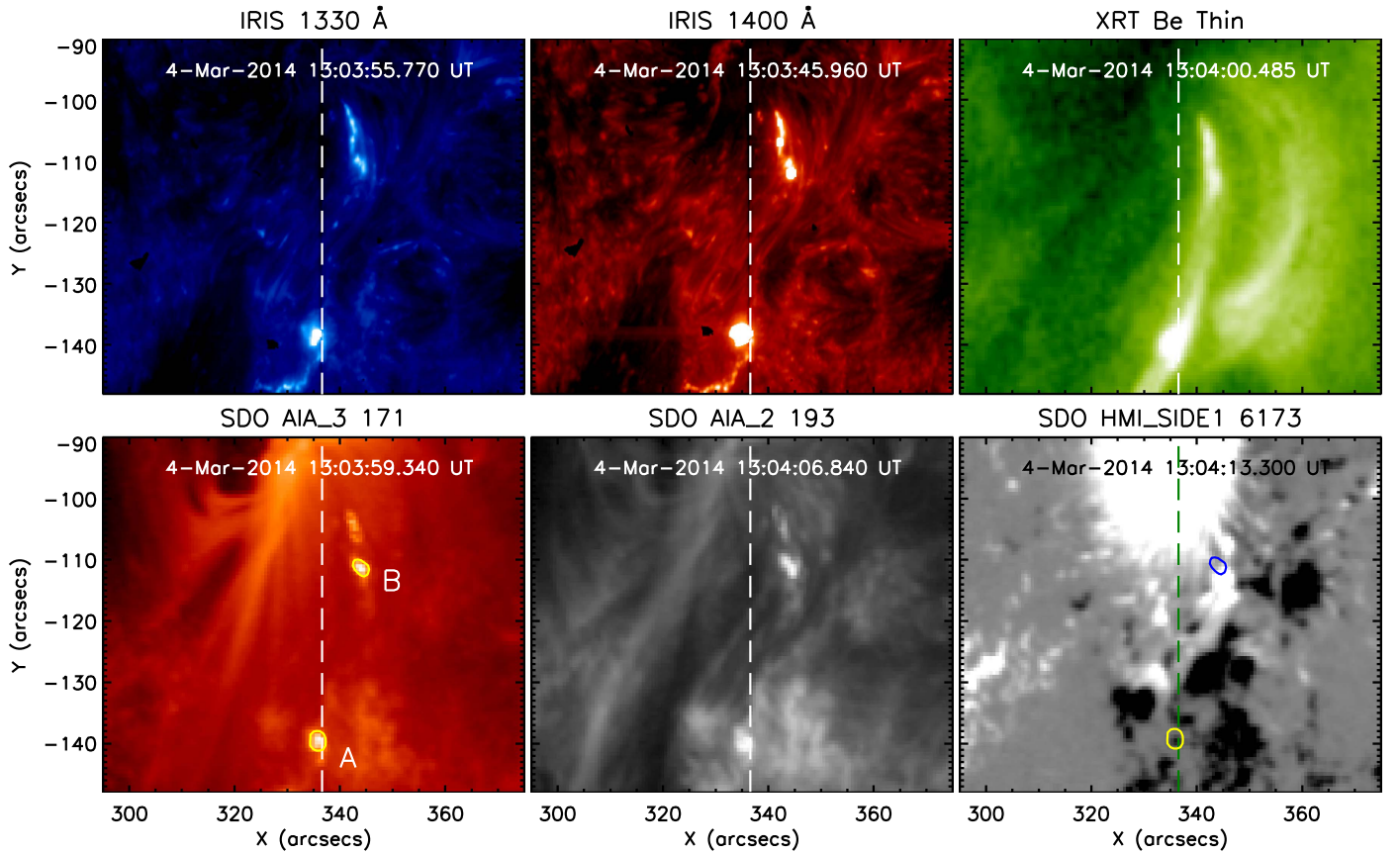


Figure 2. Images obtained from *IRIS* slit-jaw, XRT, and AIA, showing the ARTBs. The different passbands are labeled. The corresponding HMI magnetic field map scaled over ± 80 G is shown in the bottom right panel. The two contours on the HMI image indicate the brightening location obtained from the AIA 171 Å image. The vertical dashed lines on all images represent the location of the *IRIS* slit.

wavelength windows of lines C II 1335 and 1336 Å, O I 1355 Å, and Si IV 1394 and 1403 Å, whereas EIS had good signal strength only for spectral lines Fe XII 186 and 195 Å and Fe XV 284 Å among the observed lines. The exposure time for *IRIS* in spectroscopic mode was 4 s, which resulted in an effective cadence of 5 s in sit-and-stare mode. The *IRIS*-SJI observations were obtained with an exposure time of 4 s and effective cadence of 18 s, 15 s, and 15 s for SJI 1330 Å, 1400 Å, and 2796 Å, respectively. EIS spectra were obtained with an exposure time of 20 s. XRT images were obtained in several filters, such as Al_poly, C_poly, Be_thin, Be_med, Al_med, Ti_poly, and Al_thick, with varying exposure time and hence cadence. *IRIS* and AIA observations were coaligned using *IRIS*-SJI 1400 Å and AIA 1600 Å images. All of the HMI and AIA images obtained in different passbands were coaligned and derotated to the AIA 1600 Å image obtained at 12:53:28 UT using the standard procedures provided in the Solar Software package (SSW; Freeland & Handy 1998). We have used *IRIS* level-2 data where slit-jaw images from different filters and detectors are already coaligned. We used *IRIS* cool neutral line Si I 1401.514 Å to perform the absolute wavelength calibration of *IRIS* spectral lines. We followed standard procedures for calibrating the EIS data using IDL routine EIS_PREP available in the SSW. We fitted the EIS spectral line profiles with a Gaussian function using EIS_AUTO_FIT. Spatial offsets between EIS images obtained from different wavelengths were corrected with respect to the image obtained from the Fe XII 195.12 Å spectral line.

Figure 2 shows the locations of the ARTBs in *IRIS*-SJI recorded at 1330 and 1400 Å, the XRT Be-thin filter image, and AIA 171 and 193 Å images. The corresponding line-of-sight (LOS) magnetic field map obtained from HMI is plotted in the bottom right panel. “A” and “B” in the bottom left panel locate the two ARTBs that appear simultaneously. Both ARTBs appeared and peaked at the same time in different passbands of *IRIS* and AIA. Intensity contours corresponding to the ARTBs obtained from AIA 171 Å at its peak are overplotted on the HMI LOS magnetic map. The region covered by these contours shows the presence of a strong gradient in the magnetic field underneath ARTBs as compared to its surroundings. At point A, the average strength of the LOS magnetic field is about -400 G, which is surrounded by an average magnetic field strength of -50 G. Point B shows a strong gradient in the field strength, where one-half shows a field strength of 650 G and the other half 120 G. As estimates are made over only the LOS magnetic field, such a sharp gradient may indicate that these regions are possibly located in opposite polarity regions. The vertical dashed lines represent the *IRIS* spectroscopic slit that passes above the ARTB point A.

3. Data Analysis and Results

3.1. Imaging Analysis

The two ARTBs (A and B), having compact sizes of about $2'' \times 2''$, started at $\approx 13:03:11$ UT and peaked at around 13:03:45 UT. Both A and B were recorded in all of the AIA and *IRIS*-SJI passbands. Figure 3 displays the two ARTBs at

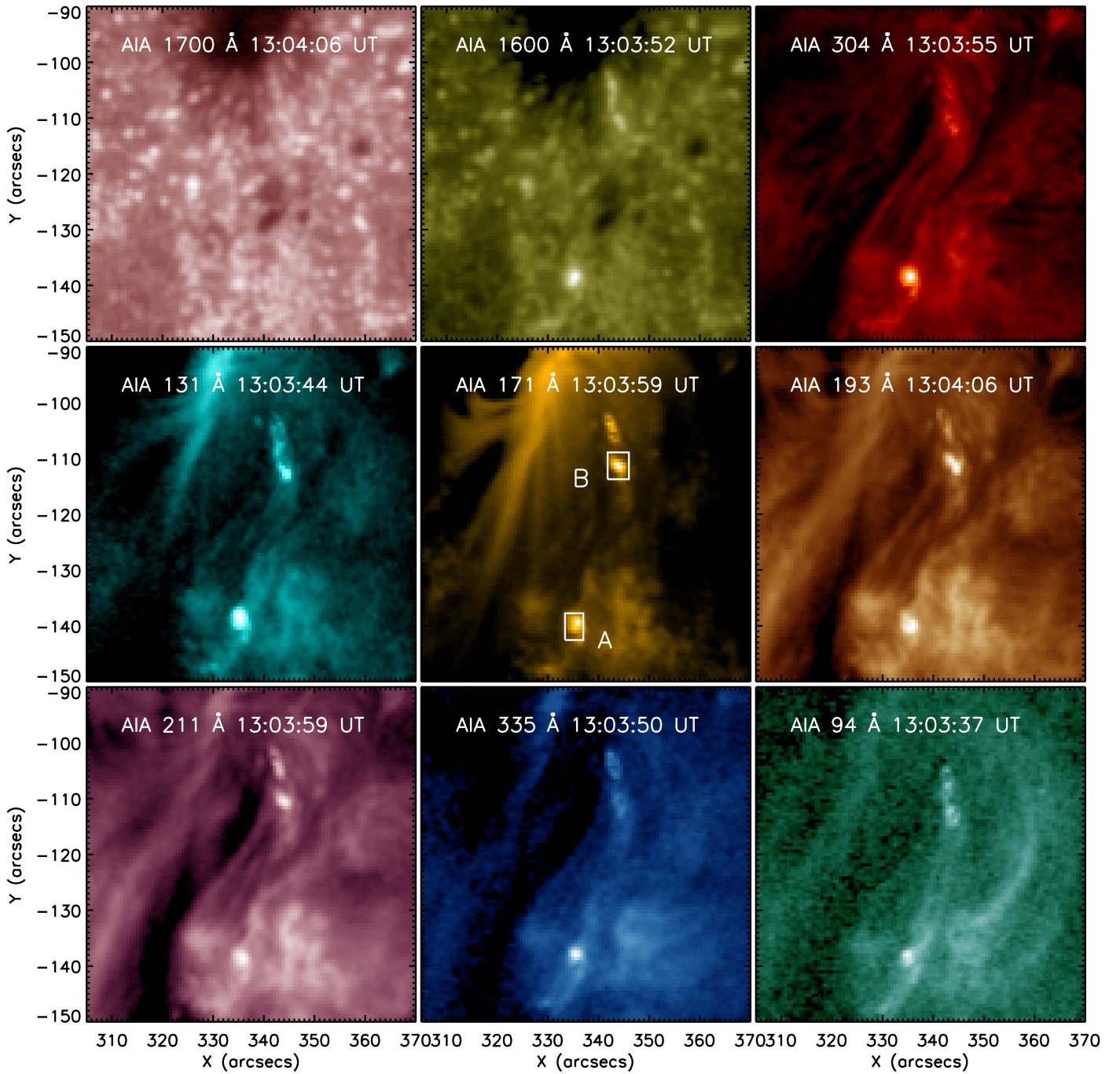


Figure 3. AIA images show the ARTBs at the peak of their life. The two boxes on AIA 171 Å locate the ARTBs as identified in the AIA 171 Å image.

their peak recorded in the AIA passbands. The ARTBs are also observed by XRT using the Be-thin filter, as shown in the top right panel of Figure 2. The two channels of AIA, namely 131 Å and 94 Å, are sensitive to hot plasma representing Fe XXI 128.75 Å and Fe XVIII 93.93 Å, respectively. However, both of these channels have strong contributions from cooler temperatures (O’Dwyer et al. 2010; Del Zanna et al. 2011). Fortunately, emission due to hot plasma corresponding to the Fe XVIII 93.93 Å spectral line from the 94 Å channel images can be separated from cool emission (Warren et al. 2012; Del Zanna 2013). In the current study, we have utilized the approach of Del Zanna (2013), where the emission due to the

hot Fe XVIII line can be obtained as

$$I(\text{Fe XVIII}) \approx I(94 \text{ Å}) - I(211 \text{ Å})/120 - I(171 \text{ Å})/450, \quad (1)$$

where $I(94 \text{ Å})$, $I(211 \text{ Å})$, and $I(171 \text{ Å})$ are intensities from the AIA 94 Å, 211 Å, and 171 Å passbands, respectively.

After the first appearance of ARTBs, a loop structure was observed at different times in different filters with the footpoints located at the two ARTBs called A and B. Figure 4 displays the hot loops seen in three AIA channels, namely AIA 335 Å, corrected 94 Å (Fe XVIII), and AIA 131 Å, and in the XRT Al_med filter. The full extent of the hot loop

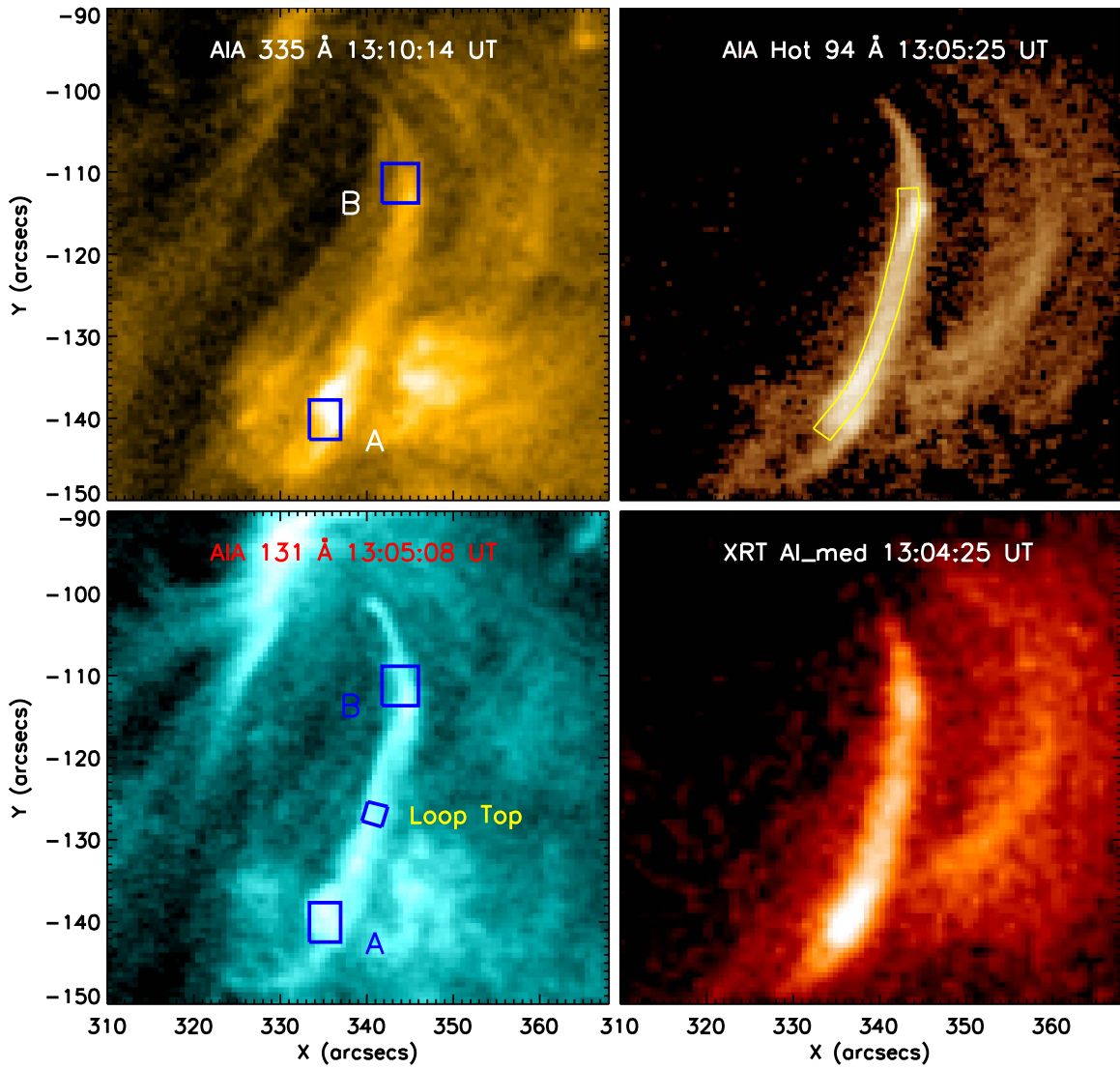


Figure 4. Brightened loop after the ARTB at the peak time of its evolution shown in the AIA 335 Å (top left), corrected 94 Å (top right), and 131 Å (bottom left) and in the XRT Al med filter (bottom right). The corrected AIA 94 Å image is obtained by subtracting the contributions from cool temperature components (see the text for details). The overplotted 5 pixel wide box in the top right panel traces the hot loop. The two blue boxes A and B locate the ARTBs, that is, the footpoints of the brightened loop, whereas the loop top is marked with the blue box as labeled.

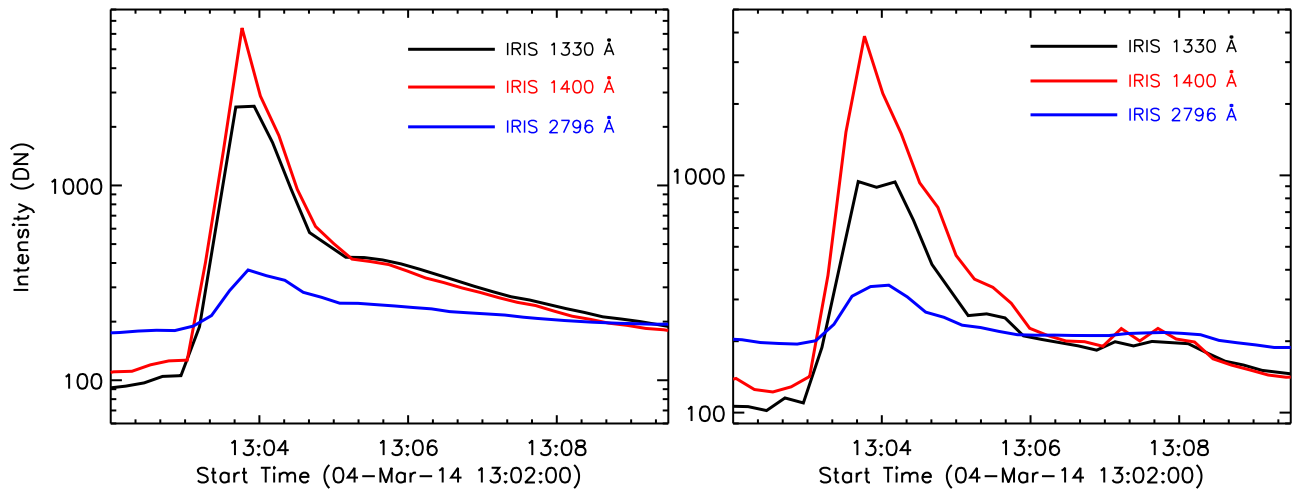


Figure 5. Light curves obtained using *IRIS*-SJI at ARTBs A (left panel) and B (right panel).

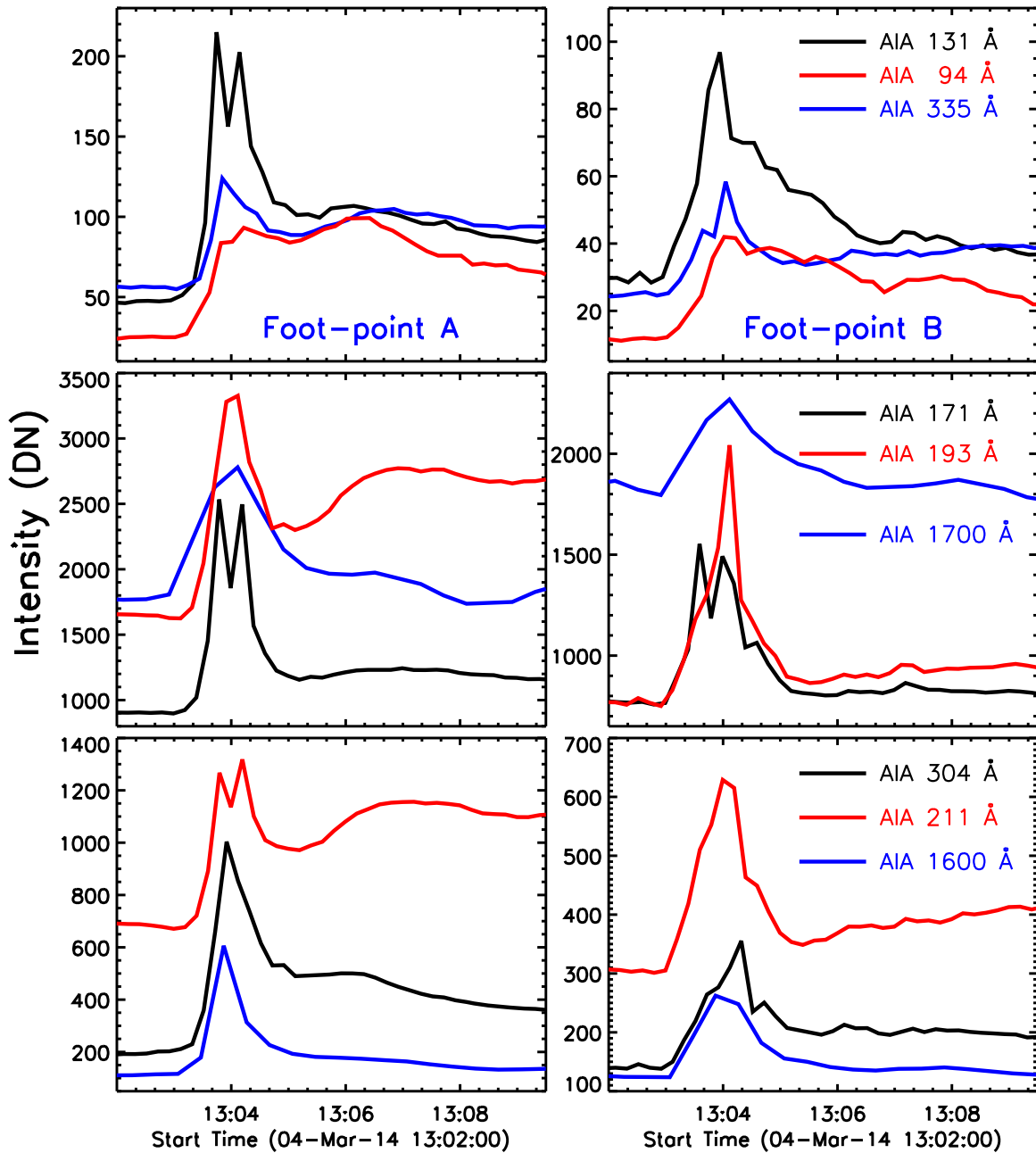


Figure 6. Light curves obtained using all of the AIA passbands corresponding to the ARTBs A (left panels) and B (right panels).

was observed in AIA 131, corrected 94, and 335 Å filters at times 13:05:08, 13:05:25, and 13:10:14 UT, respectively, whereas the peak phase of the ARTB appeared at time 13:03:44 UT, as observed from the AIA 131 Å passband. We have identified and traced the complete hot loop in the corrected AIA 94 Å (top right panel in Figure 4) passband from footpoints A to B for further analysis. The traced loop is overplotted in the top right panel of Figure 4. The width of the traced loop is chosen to be 5 pixels of AIA.

Figure 5 plots the light curves of ARTBs A (left panel) and B (right panel) obtained from all three *IRIS*-SJIs taken in 1330, 1400, and 2796 Å. For ARTB A (B), the light curves show enhancements from the initial value in the intensities by a factor of more than 25(30), 60(8), and 2(1.7) in 1330 Å, 1400 Å, and 2796 Å, respectively. It is noted that for ARTB A,

the intensity in the 1330 Å filter becomes saturated during its peak. Each of the ARTBs attained its peak within 45 s (i.e., within three time frames) of its start and became visible nearly simultaneously in all of the *IRIS*-SJIs (within the error of different observation times for different filters).

The light curves obtained for A and B using all of the AIA channels are plotted in Figure 6. As can be inferred from the plots, the intensities for both of the ARTBs are enhanced by about a factor of two to five from their initial values in different AIA passbands. Each ARTB attained its peak intensity within 36 s (i.e., within three time frames) of its start. Similar to *IRIS*, the ARTBs attained their peaks nearly simultaneously in all of the channels (within the error of different observation times for different filters). We further note here the double-peaked light curves in some channels.

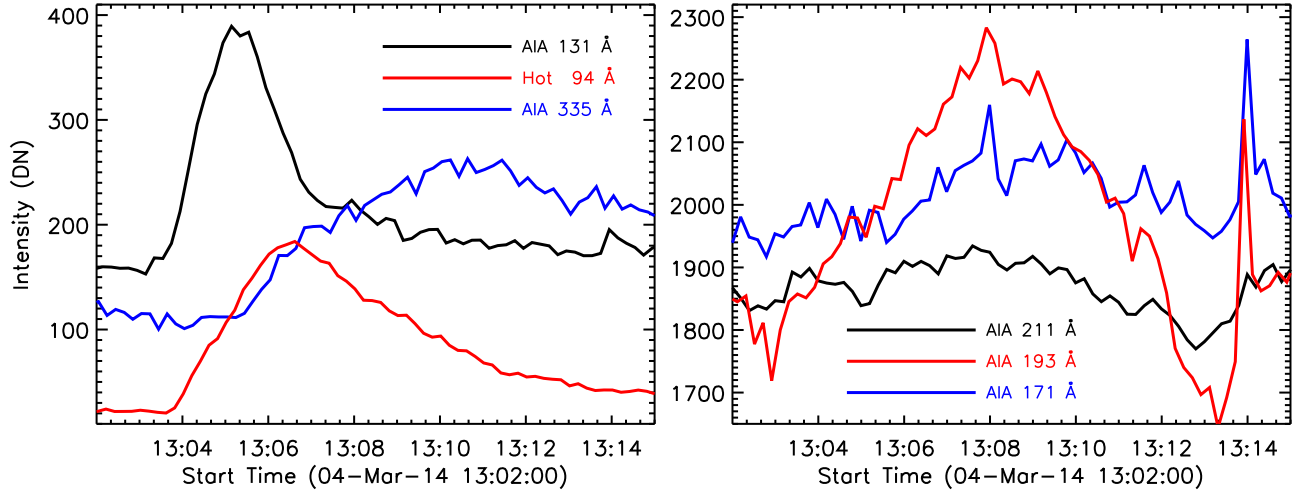


Figure 7. Light curves obtained at the loop top using all of the AIA passbands.

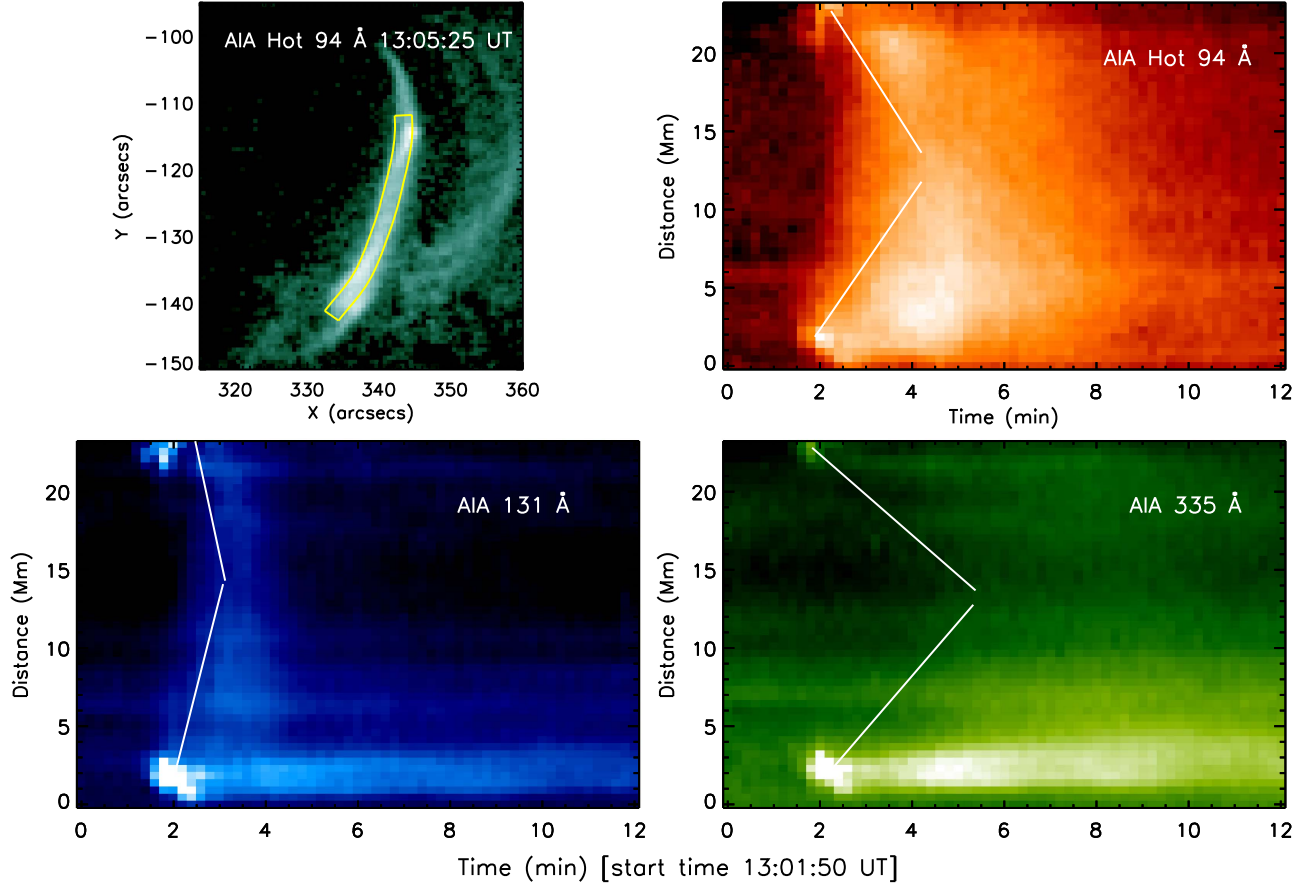


Figure 8. Top left panel: the brightened loop as observed in corrected AIA 94 Å overplotted with a 5 pixel box. The other panels show the time-distance plots obtained from corrected 94, 131, and 335 Å. The two white lines are drawn to guide the eyes to flows. Hot plasma flows from both footpoints A and B toward the loop top.

To better understand the correlation between the ARTBs (shown in Figure 3) and the appearance of the hot loops in the AIA channels (shown in Figure 4), we plot the light curves obtained at the loop top for hot channels like 131 Å, corrected 94 Å, and 335 Å in the left panel of Figure 7. The loop-top light curves for cooler channels are plotted in the right panel of Figure 7. The position of the loop top is shown in Figure 4. As can be inferred from these light curves, intensities at the loop top are enhanced by factors of about 1.4, 2.2, and 9.0 in

the AIA 335 Å, 131 Å, and 94 Å channels corrected for Fe XVIII emissions, respectively. Unlike the simultaneous appearance of the peaks of ARTBs in all of the channels of *IRIS* and AIA, the loop-top intensities in different channels attain their peaks at different times. The left panel reveals that the loop-top intensity first peaks in the 131 Å channel, followed by the corrected 94 Å and then 335 Å. The light curves for the cooler channels do not show a strong variation in the loop-top intensities.

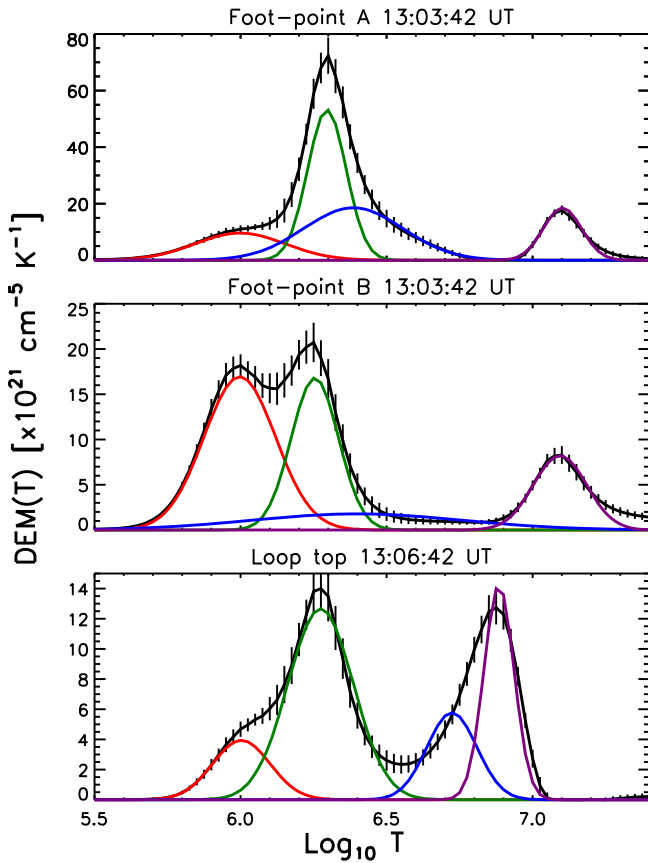


Figure 9. DEM curves obtained using six AIA coronal passbands at ARTBs A (top panel) and B (middle panel) and the loop top (bottom panel). DEM profiles are fitted with four Gaussian functions and a polynomial of degree two.

Using the traced loop shown in Figure 4, we created time–distance maps using the corrected 94 Å (top right), AIA 131 Å (bottom left), and 335 Å (bottom right) channels, and they are plotted in Figure 8. These time–distance plots clearly reveal the movement of hot plasma from the footpoint regions to the loop top. The white overplotted lines on the time–distance plots are drawn to visualize the plasma movement. The steepness of the white lines in the different time–distance plots suggests that the hot loop is first seen in the 131 Å channel, followed by the corrected 94 Å channel and later in the 335 Å channel. This is exactly as observed in the light curves shown in Figure 7. The whole loop became fully brightened after the ARTBs after ≈ 25 s in 131 Å, ≈ 40 s in 94 Å, and ≈ 6.5 minutes in 335 Å. We estimated the speed of plasma motion from footpoints toward the loop top by measuring the slope of these white lines. We found that the speed was highest in 131 Å (≈ 211 km s $^{-1}$), followed by corrected 94 Å (≈ 74 km s $^{-1}$) and 335 Å (≈ 50 km s $^{-1}$). We note that such an analysis from XRT observations was not possible as continuous observations for individual XRT filters were not available.

We further study the evolution of temperature at the locations of ARTBs as well as along the hot loop that is rooted at the two ARTBs. For this purpose, we performed a differential emission measure (DEM) analysis by employing the method of Hannah & Kontar (2012) on the six coronal channels of AIA, namely 94, 131, 171, 193, 211, and 335 Å. Figure 9 displays the DEM curves obtained at ARTBs A (top panel) and B (middle panel) and at the loop top (bottom panel)

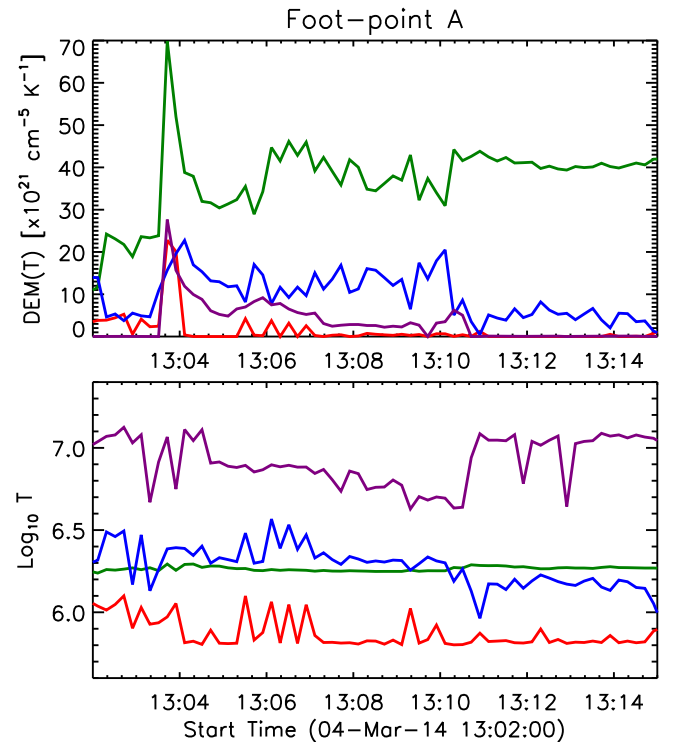


Figure 10. Time evolution of DEM components (top panel) and corresponding temperature (bottom panel) at ARTB A. The lines are color coded the same as the four Gaussian components used to fit the DEM curves shown in the top panel of Figure 9.

during their peak emission. The DEM curves obtained at both footpoints A and B show similar features with respect to temperature. The DEM curves also suggest that both ARTBs as well as the loop top show multithermal emission.

To separate out hot plasma components from the background at the footpoints and along the loop, we fitted the DEM curves with four Gaussian functions and a polynomial of degree two, similar to the approach employed by Aschwanden & Boerner (2011). The chosen function best represents the DEM curves for the desired purpose. These fitted profiles also provide the temperature of different plasma components. The four Gaussian components represent cool ($\approx 10^{5.8}$ – 10^6 K), warm ($\approx 10^{6.2}$ – $10^{6.3}$ K), intermediate ($\approx 10^{6.2}$ – $10^{6.7}$ K), and hot ($\approx 10^{6.7}$ – $10^{7.2}$ K) plasma components. These Gaussian functions representing different temperature components are overplotted with different colors in Figure 9. We use red and green colors to represent the cool and warm background plasma, respectively. The dark blue color represents newly emerged hot plasmas due to the ARTBs. The intermediate-temperature plasma component was added to obtain the best fit for the DEM curves and is represented with the blue color. Although this component is added only to fulfill the best-fit requirement, it can be interpreted as the appearance of an intermediate hot plasma component. This plasma component initially appears with the hot plasma component and later merges with the warm background plasma component.

Figures 10–12 show the time evolution of peak values of DEMs obtained at different temperature components (top panels) and associated temperatures (bottom panels) obtained at ARTBs A and B and at the loop top, respectively. The colors of the curves shown in Figures 10–12 are the same as those for the Gaussians shown in Figure 9. These curves again reveal the

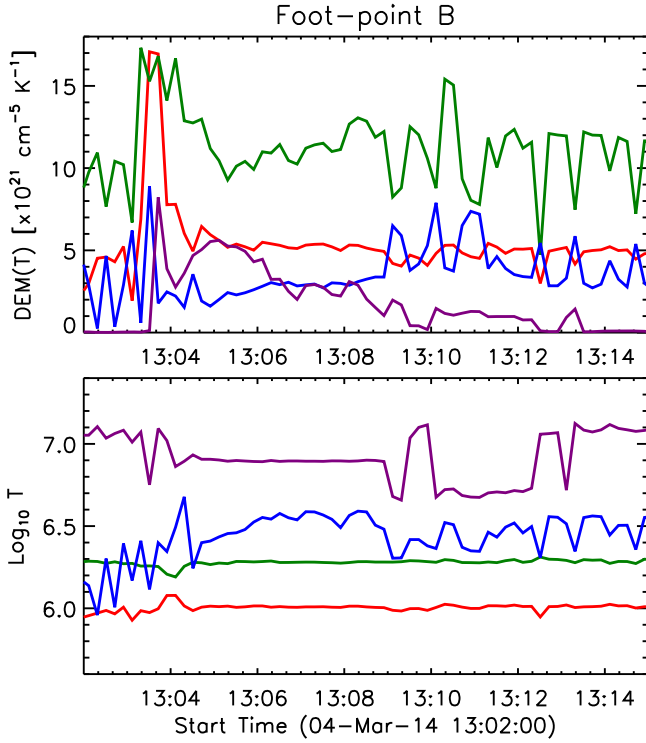


Figure 11. Same as Figure 10 but for ARTB B.

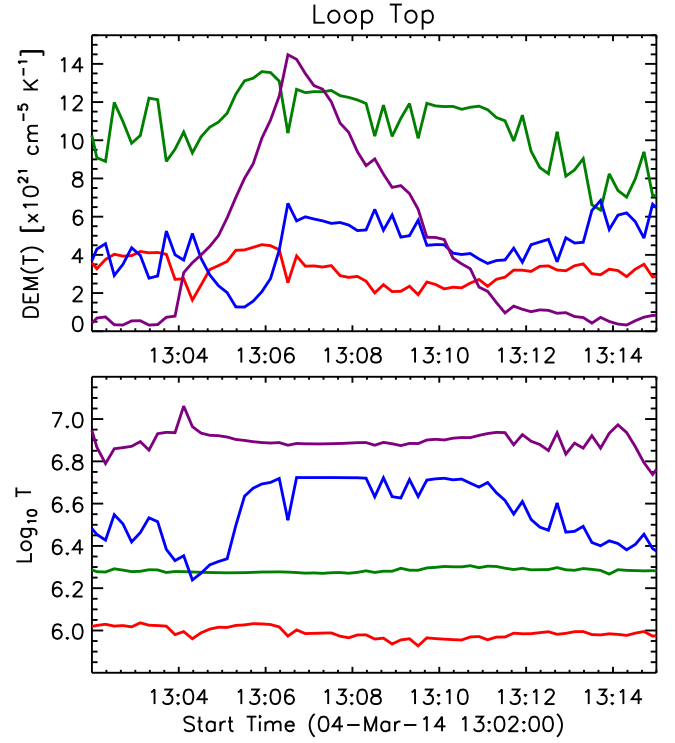


Figure 12. Same as Figure 10 but for the loop top.

existence of background cool and warm plasma components throughout the time evolution of the ARTBs A and B as well as the loop top. The emission measure (EM) from the warm plasma component is higher than that from the cool plasma throughout the evolution. The contribution from the hot plasma component due to temperature $\approx 10^{6.7}-10^{7.2}$ K appears only during the ARTB and later in the associated loop. The temperature of the hot component of the plasma changes with time. In the beginning, at the ARTBs, the plasma heats up to a temperature of $\approx 10^{7.11}$ K at 13:04:07 UT and later drops continuously afterward and reaches a temperature of $\approx 10^{6.64}$ K after about 6 minutes. The plasma at the loop top heats up to the temperature of $\approx 10^{7.06}$ K at time 13:04:07 UT and decreases to $\approx 10^{6.87}$ K within 5 minutes. However, the loop top shows the highest EM at 13:06:31 UT due to this hot component. The intermediate-temperature plasma component, which was added to obtain the best fit, did not provide any conclusive information. In this method, as noted by Sun et al. (2013), when the difference between two temperatures $T_1 - T_2$ becomes similar to the sum of two half widths at half maximum, that is, $1.31(\sigma_1 + \sigma_2)$, isolation of the two temperature components becomes difficult. In our case, it is difficult to isolate different temperature components for the footpoints A and B and the loop top beyond 13:10, 13:08, and 13:10 UT, respectively.

We also obtain the density at footpoint A using the DEM during the peak phase of the transient. We integrate the DEMs over the temperature range 10–15 MK (see top panel of Figure 9) and obtained the EM. We obtained the electron number density to be $9 \times 10^{10} \text{ cm}^{-3}$ at footpoint A by assuming a filling factor of unity and a column depth of $2''$ (which is the extent of brightening).

3.2. Spectroscopic Analysis

Fortuitously, the spectroscopic slit during the sit-and-stare observation of *IRIS* was located right above ARTB A, which allowed us to perform a detailed spectroscopic study. The top row of Figure 13 displays the line profiles before (black) and during (blue) the event in C II 1335 and 1336 Å and Si IV 1394 and 1403 Å. We fitted all of the line profiles with a single Gaussian for further analysis. Figure 13 plots the extracted parameters from fitted Gaussians, such as intensity (second row), Doppler velocity (third row), and line width (fourth row). Doppler velocity is estimated with respect to the pre-event conditions. Intensity curves (second row) for both C II and Si IV (both lines) show intensity enhancements by factors of more than 35 and 100, respectively, during the event. We also note that several pixels were saturated at time 13:03:56 UT in both of the spectral lines, indicating the epoch of peak intensity, which was attained within 40 s of its start time, as was also inferred from the *IRIS*-SJI taken in 1330 and 1400 Å.

During the event, both spectral lines of C II and Si IV show strong redshifts, with downflows of $>25 \text{ km s}^{-1}$ and $>20 \text{ km s}^{-1}$, respectively. The spectral line widths also increased from $\approx 32(40) \text{ km s}^{-1}$ in the pre-event condition to more than $65(74) \text{ km s}^{-1}$ during the event for C II 1335(1336) Å. The difference of 8 km s^{-1} in the width of two lines of C II could be attributed to the presence of several absorption features present within the wavelength span (Gupta & Tripathi 2015). The line width of the two Si IV lines increased from $\approx 35 \text{ km s}^{-1}$ to about 60 km s^{-1} . A close examination of time of enhancement in intensities, Doppler shifts, and line widths reveals that the line widths started to increase about 2–3 minutes before the start of the increase in intensities. Moreover, the Doppler shifts started to increase about a minute later than the start of increases in the line widths.

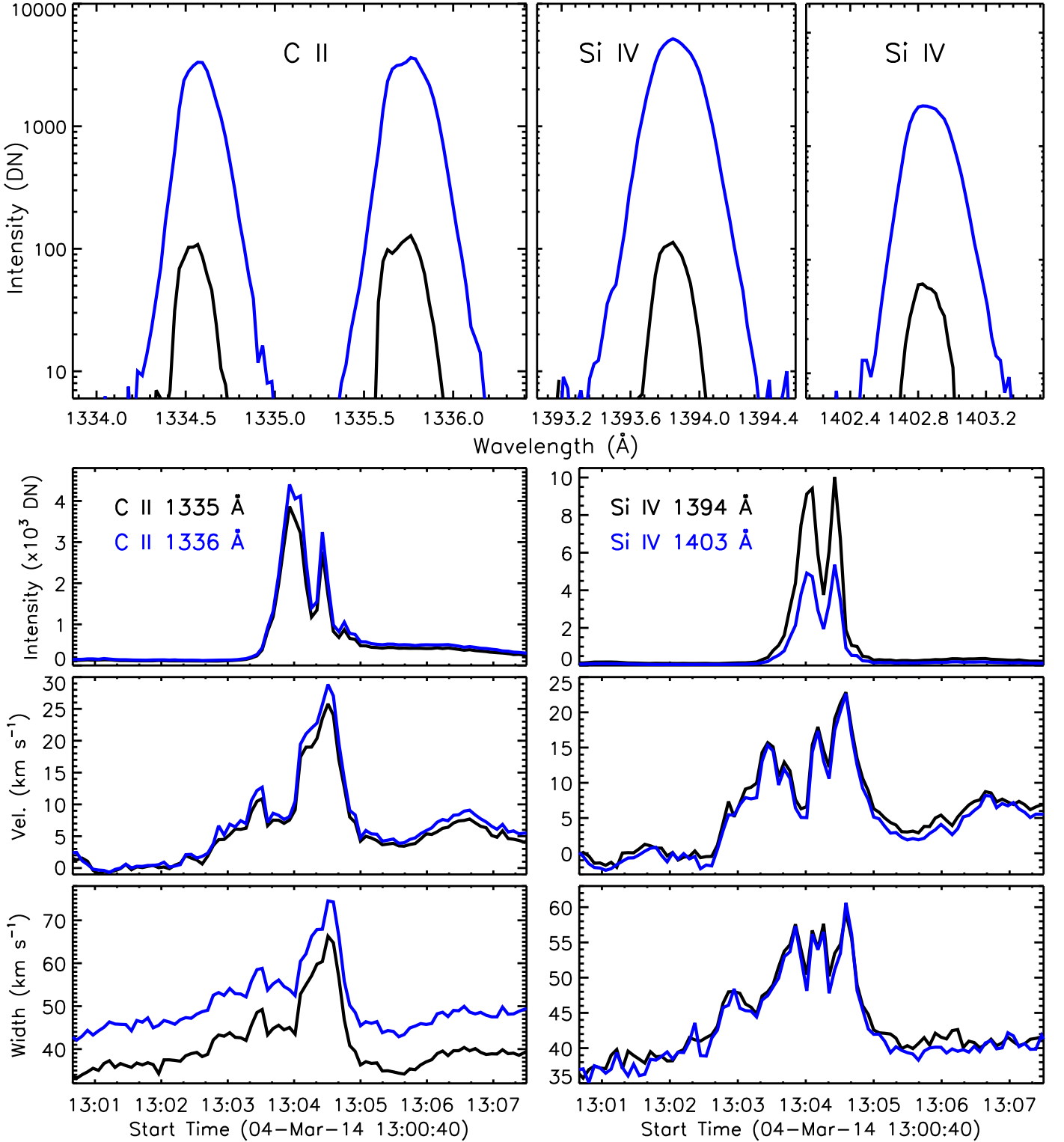


Figure 13. Top panels: *IRIS* spectral line profiles obtained from C II 1335 and 1336 Å and Si IV 1394 and 1403 Å lines before (black line) and during ARTB A (blue line). The time evolution of intensity, Doppler velocity, and line width obtained at A using both of the spectral lines are also plotted as labeled.

During the event, the spectral lines of O IV and Si IV appeared in the spectra, which were not present in the pre-event conditions. This provided us an opportunity to estimate electron densities during the event (Polito et al. 2016). For this purpose, we used the density-sensitive line pair O IV λ 1399/ λ 1401. We obtained an average line profile at ARTB A in the

time interval of 13:03:41 UT to 13:04:40 UT to improve the signal. Figure 14 shows the averaged line profiles (left panel) and theoretical intensity ratio curve as a function of electron density obtained from the CHIANTI database (right panel, Dere et al. 1997; Del Zanna et al. 2015). The O IV 1399 and 1401 Å lines are found to be blended with other cool lines in

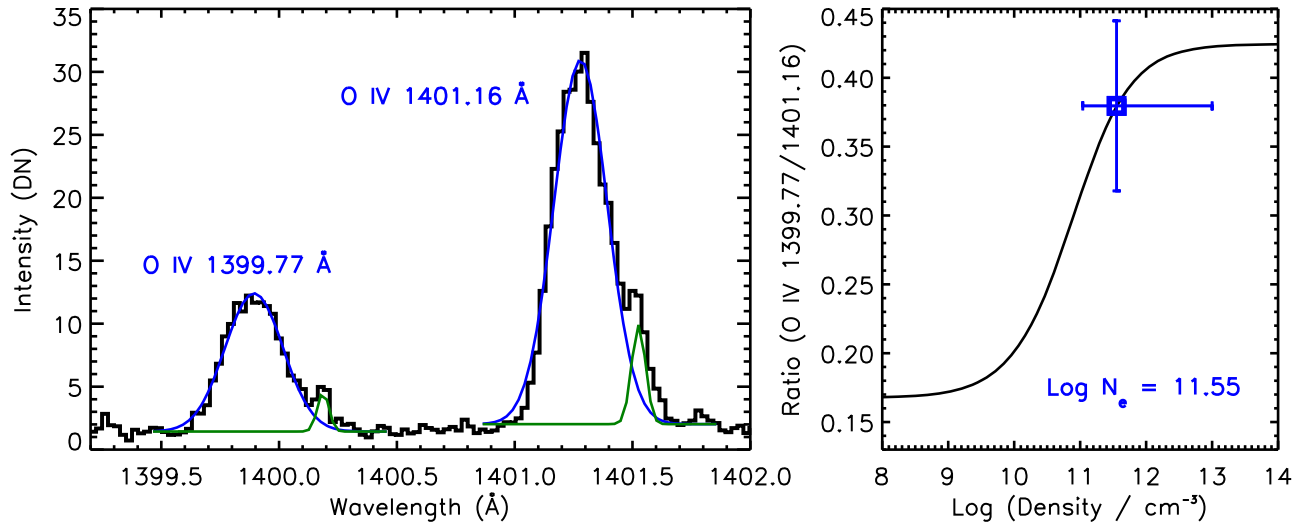


Figure 14. Average electron number density estimated at ARTB A using the *IRIS* O IV $\lambda 1399/\lambda 1401$ line pair during the transient event.

the red wings (Young 2015). Thus, to obtain the intensity of the two O IV lines, we fitted the average profiles with two Gaussian functions. Cool lines were fitted with narrow Gaussian functions with line widths near the thermal and instrumental broadening. The fitted profiles are also overplotted in the left panel of Figure 14. We obtained the intensity ratio of the O IV $\lambda 1399/\lambda 1401$ line pair, which corresponds to an electron number density of $10^{11.55} \text{ cm}^{-3}$.

The two ARTBs and the associated hot loop were also observed with EIS using a raster mode. The EIS raster started at 13:02:20 UT and ended at 13:20:23 UT. Although by using the EIS raster one cannot study the time evolution of the event, some other useful information such as electron density and flows at coronal temperatures of the event can be obtained. As the ARTBs, as well as the hot loop, were changing with time, each EIS raster step provides different information on the loop and ARTBs at different times.

Figure 15 shows the intensity maps obtained in the Fe XII 195 Å (top left) and Fe XV 284 Å (top middle) lines. The top right panel shows the electron density map obtained using the Fe XII $\lambda 186/\lambda 195$ line pair. As a raster was taken during the evolution of the loop, different phases of the loop and footpoints were observed. This makes identification of different parts of the loop difficult with respect to those observed from AIA filters. Although the loop in the EIS observation is not distinct, we attempted to trace the loop again from the EIS raster with a length equal to that of the AIA loop and overplotted it in the top panels of Figure 15. The traced loop was rastered between 13:09:33 and 13:13:10 UT. We obtained parameters such as intensity, velocity, and electron number density along the EIS loop and plotted them in the bottom panels of Figure 15. The intensity and density at both footpoints are higher than in the associated loop. The densities estimated at A and B are $10^{10.45}$ and $10^{10.15} \text{ cm}^{-3}$, respectively, whereas that near the loop top is about $10^{9.75} \text{ cm}^{-3}$. Doppler velocities were in the range of -4 to $+8 \text{ km s}^{-1}$, which is within the limits of uncertainty ($7\text{--}8 \text{ km s}^{-1}$) suggested by Young et al. (2012).

3.3. Energetics of ARTBs

Using the AIA, *IRIS*, and EIS observations, we have obtained several parameters that can be used to estimate

the order of magnitude of the energy released during the ARTBs.

Similar to Peter et al. (2014), the thermal and kinetic energy density can be written as

$$E_{\text{th}} = 3/2 n_e k_B T \quad (2)$$

$$E_{\text{kin}} = 1/2 n_e \mu v^2, \quad (3)$$

where n_e is electron number density, k_B is the Boltzmann constant, T is temperature, v is flow speed, and μ is mean molecular weight ($\approx 0.6 m_p$ for fully ionized plasma). Thus, the total energy released in volume V will be given by $V(E_{\text{th}} + E_{\text{kin}})$.

To estimate the energy released during the ARTBs, we use parameters obtained from cool transition-region lines (O IV and Si IV) during the peak phase of the transient as $n_e \approx 10^{11.55} \text{ cm}^{-3}$, $T \approx 1.4 \times 10^5 \text{ K}$, and $v \approx 20 \text{ km s}^{-1}$. We consider the volume V of the emission to be $\approx 1500 \times 1500 \times 1500 \text{ km}^3$, corresponding to a region of $2''$ cubical structure. Using these values, we find that the total energy released is $\approx 3.7 \times 10^{25} \text{ erg}$. We also estimate the total energy released at hot temperatures to be $\approx 7 \times 10^{26} \text{ erg}$ by using the parameters obtained from hot AIA channels as $n_e \approx 9 \times 10^{10} \text{ cm}^{-3}$, $T \approx 10 \text{ MK}$, $v \approx 200 \text{ km s}^{-1}$, and $V \approx 1500 \times 1500 \times 1500 \text{ km}^3$. We note here that these are just the lower limit of energy released during ARTBs, as was also pointed out by Peter et al. (2014). Estimated energies are equivalent to the energies involved in typical microflare events.

4. Comparison with Hydrodynamic Simulations

For a better understanding of the observations described in earlier sections, it is instructive to numerically simulate the scenario where a coronal loop may get brightened up following ARTBs. The observed downflows (shown in Section 3.2) in cooler lines (such as C II and Si IV) associated with ARTBs suggest a strong chromospheric condensation due to impulsive heating, similar to those observed in a flaring loop (e.g., Del Zanna et al. 2006a, 2006b; Milligan et al. 2006) or predicted by Testa et al. (2014). In this scenario, heat from the coronal part of the loop gets conducted to the chromosphere that pushes down the chromospheric plasma further during its initial phase and eventually makes it evaporate into the corona. Based on

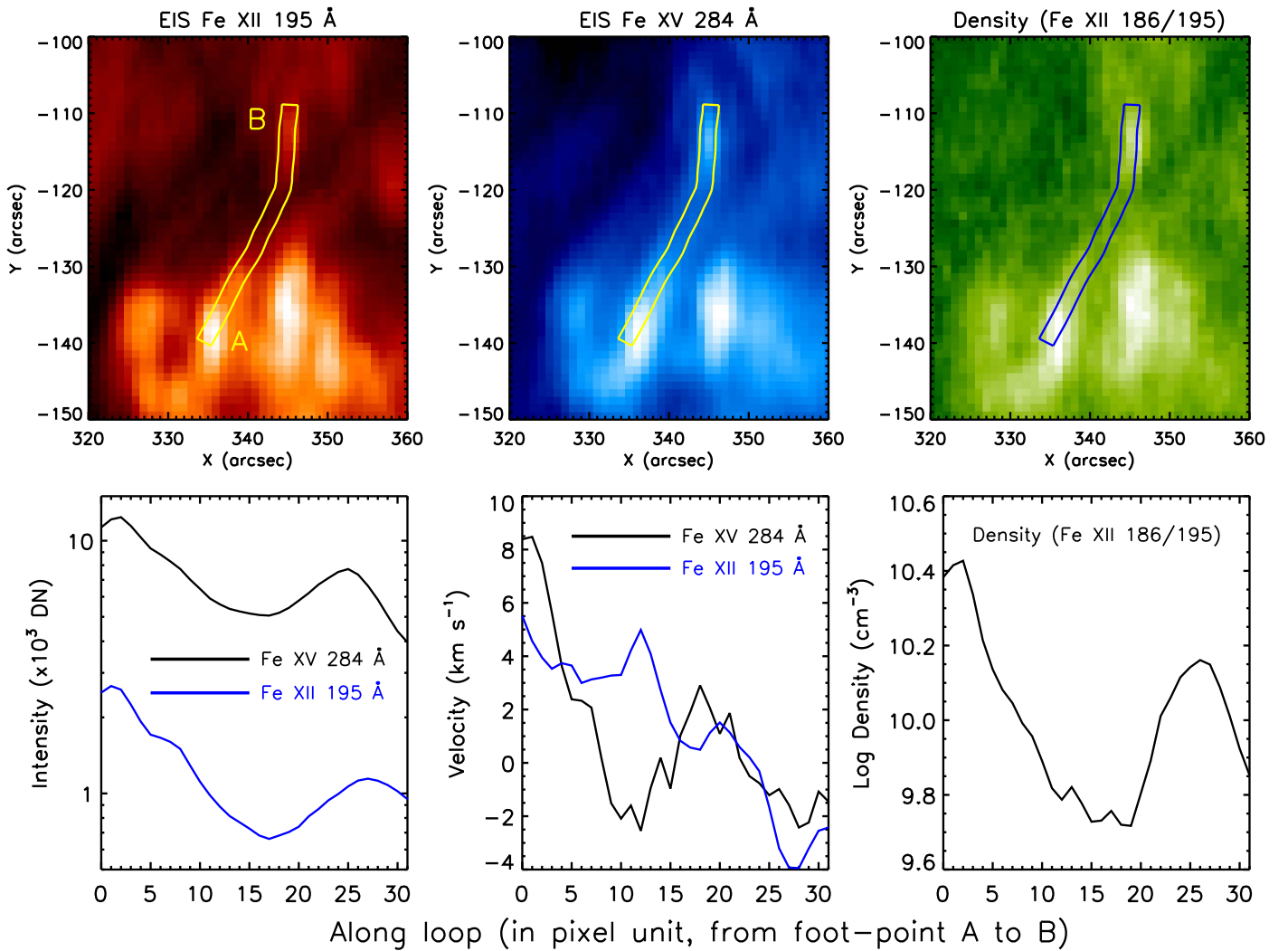


Figure 15. EIS intensity maps obtained in Fe XII 195 Å (top left) and Fe XV 284 Å (top middle), and the density map ($\log n_e = 8.5\text{--}10.5$) obtained using the Fe XII $\lambda 186/\lambda 195$ line pair (top right), as labeled. The bottom row of panels shows the variation of intensity, velocity, and electron number density along the loop length starting from A to B.

this assumption, we perform two simulations of a monolithic loop. In one of the simulations, the loop is heated by two identical microflare-like heating events of energy 10^{27} erg, while in the second one heat is deposited close to the loop top via a single microflare-like event. As we demonstrate below, the location of heating does not matter much in reproducing qualitative aspects of the observed upflow in the loop.

In order to be consistent with observations, the loop length is taken to be 24 Mm, with 20 Mm inside the corona. The loop top of the simulated loop is situated at the center of the coordinate system, whereas each end of the loop is assumed to be embedded 2 Mm into the transition region and the chromosphere to serve as a plasma reservoir. The radius of the loop is assumed to be 1 Mm. Gravity is made to change with height. The gravitational potential has the usual $1/r$ falloff with respect to the center of the Sun. The numerical details of the loop are described in Sarkar & Walsh (2009).

The initial temperature of the coronal part of the loop is taken to be 4 MK. The density profile maintains an exponential profile with the least density ($1.46 \times 10^9 \text{ cm}^{-3}$) at the loop top and the highest density ($2.45 \times 10^{11} \text{ cm}^{-3}$) toward the footpoints. We allow the loop to cool down through radiation

until 100 s, when the loop is hit by two similar heating events at the two ends of the footpoints within the corona (± 9.7 Mm). These heating events last for 120 s, span over 200 km (energy $\sim 10^{27}$ erg), and produce plasma dynamics in the loop. Panels (a) and (b) in Figure 16 depict temperature and velocity evolutions along the loop. Simulation outputs are folded through AIA response functions of 131 and 94 Å filters to produce EM outputs. To compare these EMs with real observations, we degrade the spatiotemporal resolution to 1000 km and 12 s. The resulting EM is depicted in panels (c) and (d) of Figure 16. Following the deposition of the heating events, both EM plots show a continuous brightening of the coronal loop starting at the footpoints that propagates toward the loop top. Just as in the real observations (compare Figure 8), we also mark these locations with white lines.

Soon after the occurrence of heating events at both footpoints along the coronal loop, the local plasma of the loop is heated up and pushes the transition region downward. This is evident in the temperature plot shown in panel (A) of Figure 17. Heat energy from the event sites quickly flows down to the chromosphere through conduction and leads to the evaporation of chromospheric plasma that fills up the

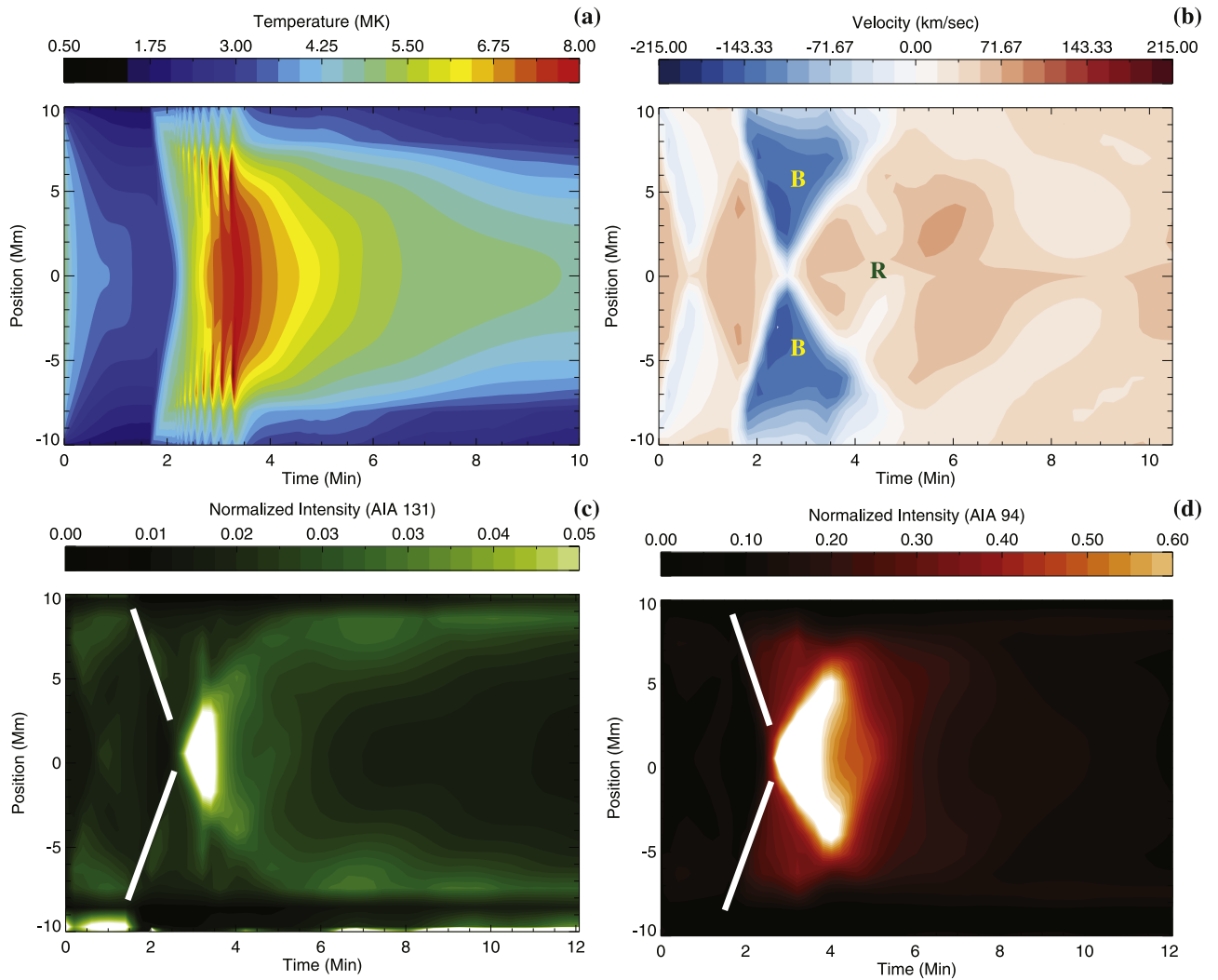


Figure 16. Evolution of simulated parameters when heat is deposited at ± 9.7 Mm: (a) temperature evolution along the loop, (b) velocity evolution along the loop, (c) synthetic AIA 131 Å emission measure, (d) synthetic AIA 94 Å emission measure.

loop, as is seen in panel (B) of Figure 17. A strong blueshifted (velocity up to 210 km s^{-1}) region is identified in panel (b) of Figure 16 (marked as B) for the same reason. Comparing panels (b) with (c) and (d) of Figure 16, one can conclude that this evaporated blueshifted plasma dictates the loop brightening from footpoints toward the loop top. Evaporated plasmas from both ends travel toward the loop top and meet each other at around 195 s, giving rise to high density at the loop top and creating loop-top brightening in the simulation, similar to the results of Sharma et al. (2016). Following the brightening, the overly dense loop top starts to condense, showing redshifted emission (marked as R in panel (b) of Figure 16). Redshifted plasma (velocity up to 65 km s^{-1}) evacuates the loop, and as a consequence the loop starts to fade away. Though we observe such downflows in the Fe XV and Fe XII lines, the measured speed ($4\text{--}8 \text{ km s}^{-1}$) is much lower than what is predicted by the simulation. The discrepancy may be due to the projection effect that is not taken into account in the simulation.

Even though we apply heat at the footpoints along the coronal loop to reproduce the observed upflow in the loop, the heating location could arguably be anywhere in the coronal part of the loop, as the conduction timescale is much faster

than the loop dynamics. Wherever heat is deposited in the corona, heat should be conducted quickly to chromosphere to evaporate plasma and should show similar dynamics in the loop. Keeping this in mind, we also apply heat close to the loop top at a single location, 1 Mm. The amount of heat deposition and other initial conditions remained the same. The result is depicted in panels (a)–(c) of Figure 18. The loop-top heating experiment predicts an initial brightening at the loop top soon after the heat deposition event, which is, however, not in accordance with the present observations. Once heat is conducted to the footpoint, a strong upflow (blueshift) is observed, as is evident from panel (b) of Figure 18. These studies therefore indicate that the location of heating does not matter much in reproducing the observed upflow in the loop. However, evidence of loop-top heating is not clear from the present observations, since there is no evidence of loop-top brightening prior to the dynamics.

5. Summary and Discussion

In this paper, we have presented a detailed study of two simultaneously occurring ARTBs with AIA-HMI/*SDO*, EIS-XRT/*Hinode*, and *IRIS*. Both ARTBs were observed in all of the passbands of AIA, *IRIS*, and XRT and attained their peak

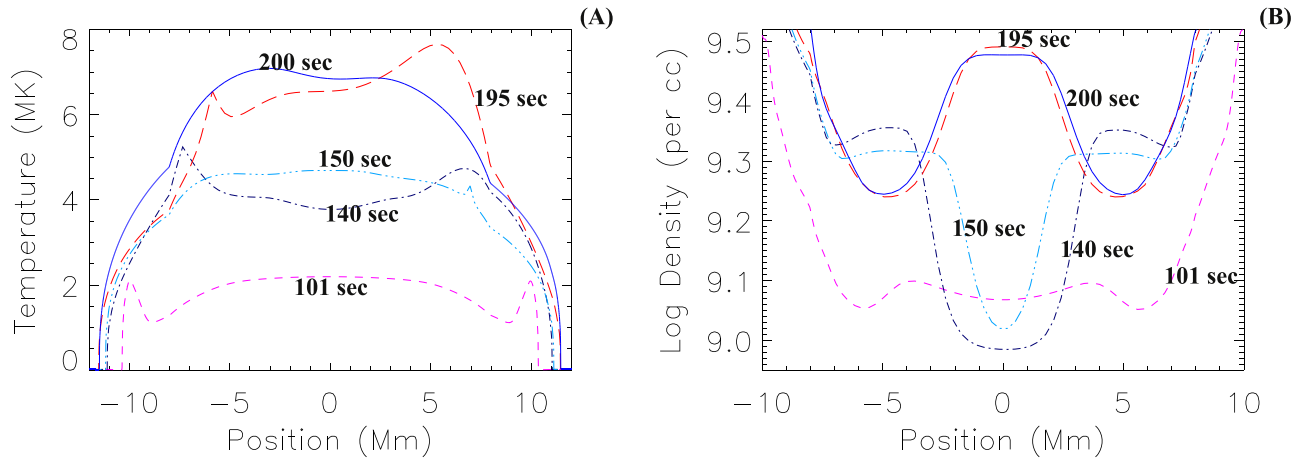


Figure 17. Evolution of (A) temperature and (B) density along the simulated loop described in Figure 16.

intensity within 36 s and 45 s in the AIA and *IRIS* passbands, respectively. In the hot channels of AIA such as 131 Å, corrected 94 Å, and 335 Å, an associated loop was seen that was rooted in the two ARTBs. The full loop became visible following the ARTBs and appeared after ≈ 25 s in 131 Å, ≈ 40 s in 94 Å, and ≈ 6.5 minutes in 335 Å. Using a time–distance plot, we detected the flow of hot plasma from the footpoints toward the loop top. The estimated flow speeds were found to be larger for a high-temperature plasma and smaller for a relatively cooler plasma.

To understand the plasma temperature of the hot loop as well as of the two ARTBs, we performed a DEM analysis using the observations taken in all six AIA coronal channels. The DEM analysis suggests that the loop, as well as footpoints, is heated up to 10 MK. Signatures of such a hot plasma are also clearly visible in the XRT images. The electron number density at ARTB A was found to be about $\approx 9 \times 10^{10} \text{ cm}^{-3}$ from the DEM analysis.

The spectroscopic study using the *IRIS* instrument that only passed through one of the ARTBs (A) revealed strong redshifts in both lines of C II and Si IV. It further revealed that the Doppler shifts at the location of the ARTB started to increase a couple of minutes earlier than the intensity. The line width started to increase even earlier. To the best of our knowledge, such an observation has not been reported earlier. Such observations may hold the key for the initiation of such events. Using the density-sensitive O IV $\lambda 1399/\lambda 1401$ line pair observed with *IRIS*, we estimated the average electron number density during the ARTB to be $\approx 10^{11.55} \text{ cm}^{-3}$.

The EIS raster, which scanned the region of interest during 13:09:33 to 13:13:10 UT, showed densities at ARTBs A and B of $10^{10.45}$ and $10^{10.15} \text{ cm}^{-3}$, respectively, whereas that near the loop top is about $10^{9.75} \text{ cm}^{-3}$. The density and temperatures obtained from the observations suggest that the total energy (kinetic and thermal) released during the transient is of the order of $\approx 10^{26}$ erg. This is similar to the energies involved in microflaring events.

The observations of downflows in cooler lines like C II and Si IV and upflows in hot AIA channels during the ARTBs can be understood by invoking the concept of a standard flare model. The upflows in the hot lines can be attributed to chromosphere evaporation, whereas the downflows in cool lines suggest chromospheric condensation (e.g., Longcope 2014; Li et al. 2017, and references therein). Figure 8 shows

that the hot loop was visible for a time interval of 2–4 minutes, 2–9 minutes, and 2–24 minutes (not shown for the full range) in the AIA 131, corrected 94, and 335 Å passbands, respectively. This finding suggests that the lifetime of the observed hot loop is temperature dependent and that the high-temperature upflows are short-lived events.

To compare the lifetime of the observed loop at different temperatures with expected cooling time due to various loss rates, we estimate a combined cooling time due to conduction and radiation as well as chromospheric evaporation given by Cargill et al. (1995):

$$\tau_{\text{cool}} \approx 2.35 \times 10^{-2} \frac{L_0^{5/6}}{T_e^{1/6} n_e^{1/6}}. \quad (4)$$

Using a half-loop length $L_0 \approx 11 \times 10^8 \text{ cm}$, temperature $T_e \approx 1 \times 10^7 \text{ K}$, and density as estimated from EIS of $n_e \approx 10^{10} \text{ cm}^{-3}$, we get $\tau_{\text{cool}} \approx 20$ minutes. This cooling time matches well with the lifetime of the loop observed from the AIA 335 Å passband.

Following Aschwanden et al. (1999), we further obtain conductive and radiative cooling time as

$$\tau_{\text{cond}} \approx 1.1 \times 10^{-9} n_e T_e^{-5/2} L_0^2 [\text{s}] \quad (5)$$

$$\tau_{\text{rad}} \approx \frac{3n_e k_b T_e}{n_e^2 \Lambda(T_e)}, \quad (6)$$

where $\Lambda(T_e) \approx 10^{-21.94} \text{ erg cm}^{-3} \text{ s}^{-1}$ for EUV loops. Using the above-mentioned observed parameters, we found $\tau_{\text{cond}} \approx 42 \text{ s}$, whereas $\tau_{\text{rad}} \approx 3607 \text{ s}$. For a temperature around 7 MK, τ_{cond} takes the value of about 100 s, whereas τ_{rad} takes the value of about 2554 s. A comparison of the lifetime of the loop with the radiative and conductive cooling times suggests that the conduction is the dominant cooling mechanism for the loop in the AIA 131 Å passband. The finding that the conductive losses are much more efficient suggest that there is more energy involved in the events than what is seen, as was also suggested by Peter et al. (2014). Similar results were obtained for Hi-C EUV bright dots studied by Subramanian et al. (2018).

To better understand the physical mechanism responsible for the observed plasma dynamics, we performed a 1D hydrodynamic simulation of a monolithic loop. In this simulation, energy was deposited at the two footpoints, mimicking the two

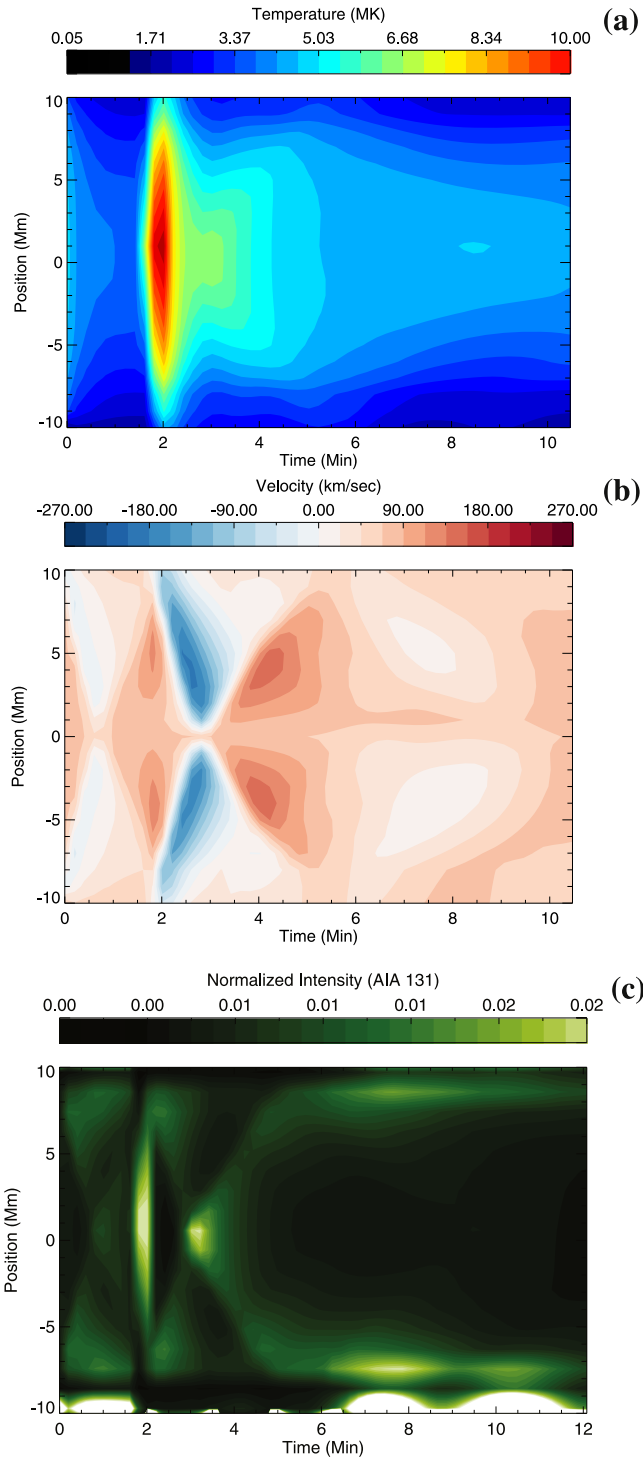


Figure 18. Evolution of simulated parameters when heat is deposited close to the loop top (at 1 Mm): (a) temperature evolution along the loop, (b) velocity evolution along the loop, (c) synthetic AIA 131 Å emission measure.

observed ARTBs. The density and temperature obtained from simulations were convolved with the temperature response function of the AIA 131 and 94 Å channels to produce intensities that would be seen in the respective channels. The simulated velocity (panel (b) in Figure 16) and the forward-modeled intensities in the 131 and 94 Å channels (panels (c) and (d) in Figure 16) closely represent the observations qualitatively. However, we see the presence of downflows in

the simulated velocities after the collision of upflows, although some downflows are present in our observations, but those are inconclusive due to limitations on the velocity measurements with EIS. Very similar dynamics are also observed when the loop is heated close to its apex, except for a loop-top brightening at the time of the heating event (Figure 18).

The enhanced EM that is observed at the loop top in forward-modeled intensities, which can be explained by the collision of the chromospheric evaporation flows (see e.g., Sharma et al. 2016), is also not present in the observation. Clearly, further observations and modeling are required to fully comprehend the dynamics of the plasma in such loop structures.

Understanding such ARTBs and their effects on mass and energy transfer in coronal loops is important because it may hold the key to coronal heating. The current observation shows that conduction is the dominant mechanism for cooling. This is suggestive of the fact that a large amount of energy is involved in such events, which is conducted away, over, and above the measured radiative energy of 10^{26} erg. Such energy may even be nonthermal in nature and could be probed with high-resolution hard X-ray instruments.

G.R.G. is supported through the INSPIRE Faculty Award of the Department of Science and Technology (DST), India. D.T. acknowledges the Max-Planck India Partner Group on Coupling and Dynamics of the Solar Atmosphere at IUCAA. AIA and HMI data are courtesy of *SDO* (NASA). *IRIS* is a NASA small explorer mission developed and operated by LMSAL with mission operations executed at NASA Ames Research Center and major contributions to downlink communications funded by the Norwegian Space Center (NSC, Norway) through an ESA PRODEX contract. *Hinode* is a Japanese mission developed and launched by ISAS/JAXA, collaborating with NAOJ as a domestic partner and NASA and STFC (UK) as international partners. The scientific operation of the *Hinode* mission is conducted by the *Hinode* science team organized at ISAS/JAXA. This team mainly consists of scientists from institutes in the partner countries. Support for the postlaunch operation is provided by JAXA and NAOJ (Japan), STFC (U.K.), NASA (U.S.A.), ESA, and NSC (Norway). CHIANTI is a collaborative project involving George Mason University, the University of Michigan (USA), and the University of Cambridge (UK).

Facility: *SDO* (AIA, HMI).

ORCID iDs

G. R. Gupta <https://orcid.org/0000-0002-0437-6107>
 Aveek Sarkar <https://orcid.org/0000-0002-4781-5798>
 Durgesh Tripathi <https://orcid.org/0000-0003-1689-6254>

References

- Aschwanden, M. J., & Boerner, P. 2011, *ApJ*, **732**, 81
- Aschwanden, M. J., Newmark, J. S., Delaboudinière, J., et al. 1999, *ApJ*, **515**, 842
- Berghmans, D., McKenzie, D., & Clette, F. 2001, *A&A*, **369**, 291
- Cargill, P. J., Mariska, J. T., & Antiochos, S. K. 1995, *ApJ*, **439**, 1034
- Chandrasekhar, K., Bemporad, A., Banerjee, D., Gupta, G. R., & Teriaca, L. 2014, *A&A*, **561**, A104
- Chifor, C., Mason, H. E., Tripathi, D., Isobe, H., & Asai, A. 2006, *A&A*, **458**, 965
- Chifor, C., Tripathi, D., Mason, H. E., & Dennis, B. R. 2007, *A&A*, **472**, 967

- Christe, S., Hannah, I. G., Krucker, S., McTiernan, J., & Lin, R. P. 2008, *ApJ*, **677**, 1385
- Culhane, J. L., Harra, L. K., James, A. M., et al. 2007, *SoPh*, **243**, 19
- De Pontieu, B., Title, A. M., Lemen, J. R., et al. 2014, *SoPh*, **289**, 2733
- Del Zanna, G. 2013, *A&A*, **558**, A73
- Del Zanna, G., Berlicki, A., Schmieder, B., & Mason, H. E. 2006a, *SoPh*, **234**, 95
- Del Zanna, G., Dere, K. P., Young, P. R., Landi, E., & Mason, H. E. 2015, *A&A*, **582**, A56
- Del Zanna, G., O'Dwyer, B., & Mason, H. E. 2011, *A&A*, **535**, A46
- Del Zanna, G., Schmieder, B., Mason, H., Berlicki, A., & Bradshaw, S. 2006b, *SoPh*, **239**, 173
- Dere, K. P., Landi, E., Mason, H. E., Monsignori Fossi, B. C., & Young, P. R. 1997, *A&AS*, **125**, 149
- Fisher, G. H., Canfield, R. C., & McClymont, A. N. 1985, *ApJ*, **289**, 414
- Freeland, S. L., & Handy, B. N. 1998, *SoPh*, **182**, 497
- Ghosh, A., Tripathi, D., Gupta, G. R., et al. 2017, *ApJ*, **835**, 244
- Golub, L., Deluca, E., Austin, G., et al. 2007, *SoPh*, **243**, 63
- Gupta, G. R., & Tripathi, D. 2015, *ApJ*, **809**, 82
- Hannah, I. G., & Kontar, E. P. 2012, *A&A*, **539**, A146
- Hudson, H., Fletcher, L., Khan, J. I., & Kosugi, T. 2004, *ASSL*, **314**, 153
- Isobe, H., & Tripathi, D. 2006, *A&A*, **449**, L17
- Klimchuk, J. A. 2006, *SoPh*, **234**, 41
- Lemen, J. R., Title, A. M., Akin, D. J., et al. 2012, *SoPh*, **275**, 17
- Li, D., Ning, Z. J., Huang, Y., & Zhang, Q. M. 2017, *ApJL*, **841**, L9
- Lin, R. P., Dennis, B. R., Hurford, G. J., et al. 2002, *SoPh*, **210**, 3
- Longcope, D. W. 2014, *ApJ*, **795**, 10
- Mariska, J. T. 1987, *ApJ*, **319**, 465
- Milligan, R. O., & Dennis, B. R. 2009, *ApJ*, **699**, 968
- Milligan, R. O., Gallagher, P. T., Mathioudakis, M., et al. 2006, *ApJL*, **638**, L117
- Mulay, S. M., Tripathi, D., Del Zanna, G., & Mason, H. 2016, *A&A*, **589**, A79
- O'Dwyer, B., Del Zanna, G., Mason, H. E., Weber, M. A., & Tripathi, D. 2010, *A&A*, **521**, A21
- Peres, G. 2000, *SoPh*, **193**, 33
- Peter, H., Tian, H., Curdt, W., et al. 2014, *Sci*, **346**, 1255726
- Polito, V., Del Zanna, G., Dudík, J., et al. 2016, *A&A*, **594**, A64
- Régnier, S., Alexander, C. E., Walsh, R. W., et al. 2014, *ApJ*, **784**, 134
- Sarkar, A., & Walsh, R. W. 2008, *ApJ*, **683**, 516
- Sarkar, A., & Walsh, R. W. 2009, *ApJ*, **699**, 1480
- Scherrer, P. H., Schou, J., Bush, R. I., et al. 2012, *SoPh*, **275**, 207
- Schou, J., Scherrer, P. H., Bush, R. I., et al. 2012, *SoPh*, **275**, 229
- Sharma, R., Tripathi, D., Isobe, H., & Ghosh, A. 2016, *ApJ*, **823**, 47
- Shimizu, T., Tsuneta, S., Acton, L. W., et al. 1994, *ApJ*, **422**, 906
- Shimizu, T., Tsuneta, S., Acton, L. W., Lemen, J. R., & Uchida, Y. 1992, *PASJ*, **44**, L147
- Subramanian, S., Kashyap, V., Tripathi, D., Madjarska, M., & Doyle, J. G. 2018, *A&A*, in press, <https://doi.org/10.1051/0004-6361/201629304>
- Sun, X., Hoeksema, J. T., Liu, Y., et al. 2013, *ApJ*, **778**, 139
- Testa, P., De Pontieu, B., Allred, J., et al. 2014, *Sci*, **346**, 1255724
- Tripathi, D., Isobe, H., & Jain, R. 2009a, *SSRv*, **149**, 283
- Tripathi, D., Isobe, H., & Mason, H. E. 2006, *A&A*, **453**, 1111
- Tripathi, D., Mason, H. E., Dwivedi, B. N., del Zanna, G., & Young, P. R. 2009b, *ApJ*, **694**, 1256
- Tsuneta, S., Acton, L., Bruner, M., et al. 1991, *SoPh*, **136**, 37
- Warren, H. P., Winebarger, A. R., & Brooks, D. H. 2012, *ApJ*, **759**, 141
- Yokoyama, T., & Shibata, K. 1995, *Natur*, **375**, 42
- Young, P. R. 2015, arXiv:1509.05011
- Young, P. R., O'Dwyer, B., & Mason, H. E. 2012, *ApJ*, **744**, 14